Investigation and Modeling of Combined Feedforward and Feedback Control Schemes to Improve the Performance of Differential Mode Active EMI Filters in AC–DC Power Converters

Rajib Goswami, *Student Member, IEEE*, and Shuo Wang, *Fellow, IEEE*

***Abstract*—In this paper, the models of active differential mode electromagnetic interference input filters for ac–dc converters are first investigated. The models are developed for active filters with single feedback (FB) and single feedforward (FF) configurations, which include an active filter, passive filters, and the noise model for a converter. To increase the gain of the single active filter, the models for FB–FF, FF–FB, parallel FB, and series feedback (SFB) configurations are developed and investigated. Loop gains and insertion gains for all of these configurations are derived and compared. Stability has been analyzed based on the loop gains and a compensation technique is introduced to ensure stability. Based on the comparison among all these control configurations, it has been found that the SFB configuration can achieve the highest noise reduction. The loop gains and insertion gains of an active filter prototype with the SFB configuration are measured using a network analyzer to validate the developed model and compensation technique. Finally, spectrum measurements with a commercial boost power factor correction ac–dc converter have been conducted to verify the developed modeling and control techniques as well as the predicted performance for the SFB configuration.**

***Index Terms*—AC–DC converters, active filter, differential mode (DM) noise, electromagnetic interference (EMI), feedback (FB), feedforward (FF).**

I. Introduction

MODERN switching mode power converters generate electromagnetic interference (EMI). With increased power density, EMI issue is becoming severe day by day [1]. EMI filters are used to attenuate EMI and meet the different EMI standards. Passive filters constituting inductors and capacitors are most commonly employed to solve EMI issues, but in case of differential mode (DM) noise, the DM capacitors must have enough voltage ratings and the DM inductors must carry full load current and hence, the size of the passive DM filters can be big.

Hybrid EMI filters, including a small passive filter and an active filter, have been extensively investigated in the available literature [1]–[18] to reduce the overall size of the EMI filter. But, most of the literature deals with common mode (CM) noise [1]–[16]. For DM noise, active filters have been investigated mostly for dc–dc converters [17]–[20]. Few papers, such as [21]–[24], [32], and [33], dealt with hybrid DM EMI filters in ac–dc converters. But these papers have shown that implementing active DM filters on ac side is very challenging compared to CM active filters and DM active filters on dc side. Active filters sense noise voltage or current and inject voltage or current to cancel the noise. For DM active filter, while sensing the DM noise, the DM power-line frequency voltage or current is sensed along with DM EMI noise [21]–[24]. For CM active filter, the CM noise sensing part cancels all the DM signals including the power line frequency voltage/current and DM EMI noise [1]. Hence, it can sense CM noise only [1]. For dc–dc converters, the dc voltages or currents can be easily removed from the sensed noise signal [17]–[20]. On the other hand, the DM active filter on the ac side must have a high-order high-pass filter (HPF) to reject the power-line frequency voltage or current from the sensed DM signal as they are not supposed to be canceled. However, it is very difficult for the DM active filter to maintain a very low gain at the power-line frequency and a high gain at the beginning of the concerned EMI frequency range, in which the highest EMI is usually located, as there are only a few decades distance between these frequencies. While trying to maintain substantial midband gain as well as sufficiently low gain at power-line frequencies, an unavoidable sharp gain rise is required for the active filter before the midband. This introduces stability issues [21] and is very difficult to solve. In [23] and [33], a feedback (FB) active filter circuit has been developed to reduce the DM EMI of ac–dc converters, but due to low gain requirement at line frequency and the stability constraints at both low and high frequencies, the single FB active filter cannot

Manuscript received December 22, 2017; revised April 19, 2018, June 12, 2018, September 10, 2018, and October 9, 2018; accepted October 30, 2018. Date of publication December 11, 2018; date of current version March 29, 2019. This work was supported by National Science Foundation under Award Number 1540118. *(Corresponding author: Shuo Wang.)*

R. Goswami is with the Electrical and Computer Engineering Department, University of Texas at San Antonio College of Engineering, San Antonio, TX 78249 USA (e-mail: rajibshohag@gmail.com).

S. Wang is with the Electrical and Computer Engineering Department, University of Florida, Gainesville, FL 32611 USA (e-mail: shuowang@ieee.org).

Color versions of one or more of the figures in this paper are available online at http://ieeexplore.ieee.org.

Digital Object Identifier 10.1109/TIE.2018.2883264

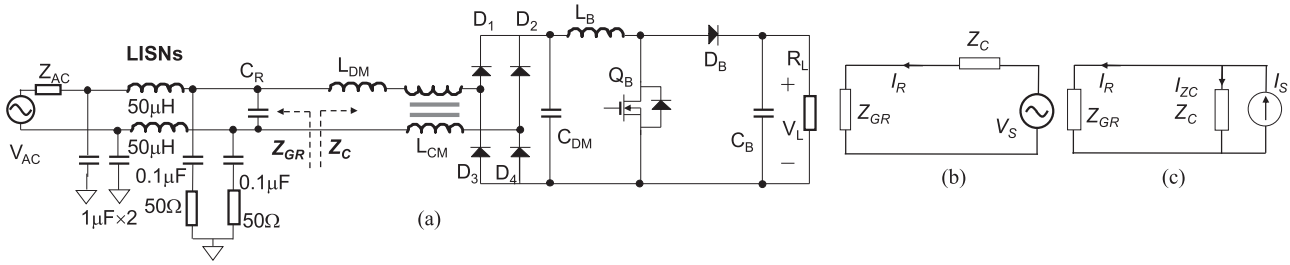

Fig. 1. (a) Boost PFC ac–dc converter with passive EMI filters. (b) DM EMI noise model with the Thevenin equivalent noise source, and (c) with the Norton equivalent noise source.

achieve very high gain to greatly reduce DM noise. Until now, for the single active DM EMI filters in ac–dc converters, detailed mathematical modeling and hardware design techniques to solve all the associated issues while achieving very high gains are not found in the available literature. Hence, for the DM active filters of ac–dc converters, different control configurations and the modeling and design techniques need to be investigated to increase the gain of the single FB DM active filters and this work is not done in any previous literature.

In this paper, at first, at the noise source end, DM noise model including an ac–dc converter and existing passive filter components is developed and, at the noise receiving end, the DM noise model including both line impedance stabilization networks (LISNs) and passive filter components is developed. Second, the models of all the active filter components were developed. Component level models were first developed similar to work presented in [3], [22], and [32] and later they were verified through experiments. Third, combining the component level models, based on the single FB active filter circuits proposed in [23] and [33], the active DM EMI filter models in single FB and single feedforward (FF) configurations are developed including the models of a noise source, a passive filter, and a load. Fourth, to improve the single active filter's gain, close loop models for FF–FB, FB–FF, parallel feedback (PFB), and series feedback (SFB) active filter configurations are developed. To achieve the best performance, the insertion gains and loop gains of these control configurations are developed and compared, and their stability has been analyzed. Compensation techniques were developed to ensure stability. It has been found that the insertion gain improvement of FF–FB and FB–FF topologies over single FB configuration mostly depend on the FF active filter's gain and the performance is not as good as expected due to the inaccuracy of the component values. On the other hand, the SFB configuration can give a much better insertion gain than all other configurations. Its compensation technique is also simple and similar to that of a single FB active filter. The loop gains and insertion gains of the SFB configuration have been measured to verify the modeling and compensation techniques. Finally, to validate the developed modeling and stability analysis techniques, experiments were conducted, first, with a signal generator and then with a commercial ac–dc boost power factor correction (PFC) converter as a noise source.

The specific contributions of this paper to the DM active EMI filters of ac–dc converters are listed as follows. The models of FF, FF–FB, FB–FF, PFB, and SFB active filters are investigated and accurately developed for the first time in the available literature. Also, for the first time in the available literature, the insertion gain and loop gain equations for FF, FF–FB, FB–FF, PFB, and SFB active filter control configurations are developed, their stability is analyzed, and compensation techniques are proposed to ensure stability. After comparing these developed models, a solution to overcome the challenges and constraints of single FB DM active EMI filter is proposed by successfully designing and implementing the SFB active filter, which has much superior insertion gain compared to other configurations. It has been proven through experiments that the models developed in this paper can correctly predict active filter's performance and stability. The compensation techniques developed based on these models can ensure stability. It has also been verified through spectral domain measurements that the developed SFB configuration gives significantly better performance than the single FB active filter, which is an important improvement for the DM active EMI filter design for ac–dc converters.

II. FF and FB Active Filters to Reduce the DM Noise of ac–dc Converters

A. DM Noise Source and Load Modeling

In Fig. 1(a), a boost (PFC) ac–dc converter, connected to an ac source V_{AC} via LISNs, is shown along with passive EMI filter components. L_B is the boost inductor. C_{DM}, L_{CM}, L_{DM}, and C_R are passive filter components. C_{DM} and C_R are DM filter capacitors, L_{DM} is a DM filter inductor, and L_{CM} is a CM inductor, which has a leakage inductance of L_{DM_CM}. The ac source has impedance $Z_{AC}(s)$. The equivalent impedance looking into the converter on the right of the passive filter capacitor C_R is $Z_C(s)$ and the impedance looking into the grid side including C_R is $Z_{GR}(s)$. In [27] and [29], it has been shown that the DM noise model of a single-phase boost PFC ac–dc converter can be represented by a Thevenin equivalent noise voltage source with a source impedance equivalent to boost inductor's impedance. This is because, while modeling the equivalent DM noise impedances, the diode bridge can be considered as short circuit because of the PFC operation and the semiconductor switch Q_B can be considered as a voltage source based on substitution theory [29]. Based on this, $Z_C(s) = Z_{LDM}(s) + Z_{LDMCM}(s) + Z_{CDM}(s)||Z_{LB}(s)$ and $Z_{GR}(s) = Z_{CR}(s)||Z_{LISN}(s)$, where $Z_{LDM}(s)$ is the impedance of DM inductor L_{DM}, $Z_{LDMCM}(s)$ is the impedance of the leakage

inductance $L_{\text{DM\_CM}}$, $Z_{\text{CDM}}(s)$ is the impedance of capacitor C_{DM}, $Z_{\text{LB}}(s)$ is the impedance of the boost inductor L_B, $Z_{\text{CR}}(s)$ is the impedance of capacitor C_R, and $Z_{\text{LISN}}(s)$ is the DM impedance of the two LISNs. In the concerned EMI frequency range, $Z_C(s)$ is mostly determined by the DM inductor and CM inductor's leakage inductance impedance $Z_{\text{LDM}}(s) + Z_{\text{LDMCM}}(s)$ and hence, $Z_C(s) \gg Z_{\text{GR}}(s)$, as $Z_{\text{GR}}(s)$ is mostly determined by the capacitor C_R's impedance $Z_{\text{CR}}(s)$. The active filter will later be inserted between $Z_{\text{GR}}(s)$ and $Z_C(s)$ as the impedance mismatch requirement [1] for the active filter requires big source impedance and small load impedance at this node.

Based on the Thevenin theorem, the DM noise model can be represented with a Thevenin equivalent noise voltage source $V_S(s)$ in series with an equivalent impedance $Z_C(s)$, as shown in Fig. 1(b). In Fig. 1(c), the model is shown with a noise impedance $Z_C(s)$ in parallel with a noise current source $I_S(s)$ based on the Norton theorem. The load impedance is represented by $Z_{\text{GR}}(s)$ in both cases. In Fig. 1(b) and (c), the noise current flowing through the load is $I_R(s)$. In Fig. 1(c), the open-loop gain $G_{\text{OL}}(s)$ of the passive filter is defined as the current gain from the DM noise current source $I_S(s)$ to $I_R(s)$

$$G_{\text{OL}}(s) = \frac{I_R(s)}{I_S(s)} = \frac{Z_C(s)}{Z_C(s) + Z_{\text{GR}}(s)}. \tag{1}$$

B. FF and FB Active Filters

An active EMI filter has three basic function blocks: noise sensing, amplification, and noise injection. Depending on noise sensing and injection techniques, an active filter can be of four different configurations [6]: voltage sensing–voltage injection, voltage sensing–current injection, current sensing–current injection (CS–CI), and current sensing–voltage injection.

A voltage injection active filter needs one voltage transformer in series with converter's ac power delivery path. The voltage transformer generally has big size because its windings carry full power currents and it must have enough magnetizing inductance to limit the extra power loss introduced by magnetizing currents to the active filter. This reduces the advantage of using active EMI filters. Hence, current injection is chosen for both the FB and FF active filters.

For noise sensing, current sensing is preferred over voltage sensing, as it is convenient to separate DM noise currents from CM currents using a current transformer (CT), which can also provide a high gain through its load resistor, unlike the voltage sensing using a voltage divider where the gain is less than one. With the increased noise sensing gain, the gain requirement to the active filter's amplifier is alleviated so it can have higher bandwidth as its product of gain bandwidth is constant. Hence, CS–CI active filter configuration is selected in this paper.

A CS–CI active filter can be implemented either in FF or in FB control configuration. Fig. 2(a) shows an active filter with FF control configuration and Fig. 2(b) shows an active filter with FB control configuration. Z_{outFF} and Z_{outFB} are the output impedance of the active filters. Z_{injFF} and Z_{injFB} are the injection network impedance of the active filters. I_{CancelFF} and I_{CancelFB} are the injected noise cancelation currents due to the output voltage added to the equivalent load impedances of the active filters.

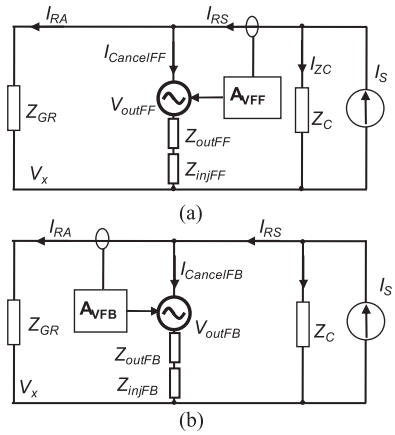

Fig. 2. CS–CI active filter in (a) FF and (b) FB configuration with the Norton equivalent DM noise model of an ac–dc converter.

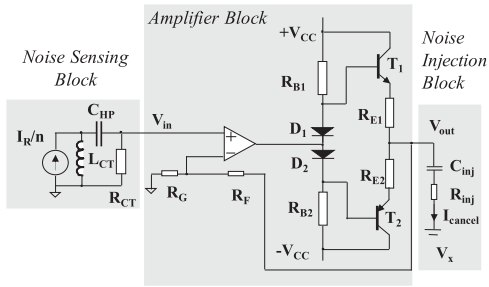

Fig. 3. CS–CI active filter circuit with three function blocks.

A_{VFF} and A_{VFB} are the current to voltage gains of the active filters from the sensed current to the output voltage of the active filters.

In Fig. 2, the CS–CI active DM EMI filter is added between L_{DM} and C_R in Fig. 1(a). Because the DM active EMI filter only injects cancelation current in the EMI frequency range, which is much higher than the converter's control loop bandwidth, it does not influence converter's stability. Furthermore, the passive DM filter between the active filter and the converter can decouple the active filter from the ac–dc converter.

The active filter circuit [33] in Fig. 3 is used for the investigation of CS–CI filter in Fig. 2(a) and (b), along with the three function blocks described above. The CS–CI FB active filter in Fig. 3 consists of current sensing, amplifier, and current injection blocks. The active filter for ac–dc converters must have an HPF to reject the low frequency line currents, but this introduces stability issues due to its phase shift. In the current sensing block, CT can be modeled as a current source I_R/n in parallel with CT's secondary inductance L_{CT} (neglecting parasitic components) [3]. CT's load resistance is R_{CT} and turns ratio is n. C_{HP}, L_{CT}, and R_{CT} constitute an HPF to reject line frequency currents with high attenuation. The corner frequency of the HPF can be controlled via C_{HP}, and an appropriate corner frequency of HPF can help achieve enough phase margin of the loop gain at low frequency crossover to achieve stability [32].

A noninverting operational amplifier (OPAM) voltage amplifier configuration [23], [33] is used in the amplifier block. The FB impedances Z_G and Z_F are used to achieve the necessary

gain and phase margin for active filter's loop gain. A class AB amplifier is added at the output of the OPAM to increase the noise cancelation current injection capacity [33]. The emitter resistors R_{E1} and R_{E2} are used to solve the thermal runaway issue. R_{B1} and R_{B2} are the base resistors used for biasing the class AB amplifier. D_1 and D_2 are biasing diodes.

To inject the DM cancelation current, injection capacitor C_{inj} and a small resistor R_{inj} are added to the output of the voltage amplifier, as shown in Fig. 3. The impedances of C_{inj} and R_{inj} are Z_{injFF} and Z_{injFB} in Fig. 2. The injection capacitor is needed to isolate the active filter from high voltage and the resistor is needed to ensure stable impedance at the pass band. The open-loop transfer function A_{VFB} for the FB active filter or A_{VFF} for the FF active filter from the sensed primary current I_R in CT to the output voltage V_{out} can be modeled as [32]

$$A_{\text{VFB}} \text{ or } A_{\text{VFF}} = \frac{V_{\text{out}}}{I_R} = \frac{V_{\text{in}}}{I_R} \times \frac{V_{\text{out}}}{V_{\text{in}}} = \frac{2 \times \left(\frac{s}{\omega_{\text{HP}}}\right)^2 \frac{R_{\text{CT}}}{n}}{1 + \frac{s}{\omega_{\text{HP}} Q} + \left(\frac{s}{\omega_{\text{HP}}}\right)^2} \times \frac{\frac{G_{\text{OPC}}}{Z'_o}}{\frac{1}{Z'_o} + \frac{1}{R_G + R_F} + \frac{R_G}{R_G + R_F} \times \frac{G_{\text{OPC}}}{Z'_o}} \tag{2}$$

where V_{in}/I_R and $V_{\text{out}}/V_{\text{in}}$ are CT and amplifier blocks' transfer functions, respectively. Also, $\omega_{\text{HP}} = 1/(L_{\text{CT}} C_{\text{HP}})^{1/2}$ and $Q = (L_{\text{CT}}/C_{\text{HP}})^{1/2}/R_{\text{CT}}$ [23]. The model of the CT, given by the transfer function V_{in}/I_R, and the model for the OPAM, given by the transfer function $V_{\text{out}}/V_{\text{in}}$, are directly given here. They are derived similar to the method used in [3], [22], and [32] and are not shown here in detail due to brevity.

The voltage gain G_{OPC} of the amplifier block is

$$G_{\text{OPC}} = \frac{V'_{\text{OP}}}{V_{\text{in}}} = \frac{K_P \times G_o}{\left(1 + \frac{s}{\omega_{\text{OP1}}}\right)\left(1 + \frac{s}{\omega_{\text{OP2}}}\right)\left(1 + \frac{s}{\omega'_{\text{PBC}}}\right)}. \tag{3}$$

G_{OPC} is derived similar to that in [3] and the derivation of this model is not shown here for brevity. In (3), the poles ω_{OP1} and ω_{OP2} are OPAM's open-loop poles, which can be derived from its datasheet. The pole ω_{PBC}' is generated by the class AB amplifier transistor's base to collector junction capacitance C_{BC} and equivalent resistance R_B at the base. ω_{PBC}' is a very high frequency (HF) pole and can be neglected for the concerned frequency range from 10 kHz to 30 MHz. G_o is OPAM's open-loop dc gain and K_p is the voltage gain of the class AB amplifier. Because the class AB amplifier works in a voltage follower configuration, $K_p \approx 1$. Z'_O is the open-loop output impedance of the amplifier block and $Z'_O = R_E + (R_O + R_{\text{BE}})/(\beta + 1)$, where R_o is the open-loop output resistance of the OPAM. $R_E = R_{E1} = R_{E2}$ is the emitter resistance, R_{BE} is the base to emitter small signal resistance of the transistor, and β is the current gain of the transistor.

C. Closed-Loop Model of FF and FB Active Filters

A signal flow diagram for the FF active filter of Fig. 2(a) is shown in Fig. 4(a) based on circuit equations and signal flow theory. The signal flow diagram in Fig. 4(a) can be further reduced to Fig. 4(b) based on signal flow theory. The reduced

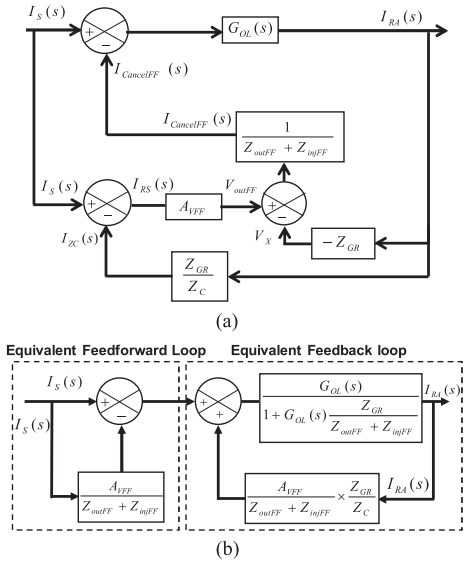

Fig. 4. Signal flow diagram for the FF active filter in Fig. 2(a). (a) Original signal flow graph and (b) reduced signal flow graph.

signal flow graph in Fig. 4(b) has an equivalent FF loop and an equivalent FB loop. In FF loop, $A_{\text{VFF}}/(Z_{\text{outFF}}+Z_{\text{injFF}})$ should be close to one for the maximum cancelation of the noise current $I_S(s)$. The FF loop is always stable if A_{VFF} itself is stable, and hence the overall stability depends on the FB loop. The loop gain of the FB loop of the closed-loop FF active filter is therefore

$$T_{\text{FF}} = \frac{-A_{\text{VFF}}(s)}{Z_{\text{outFF}} + Z_{\text{injFF}} + Z_C || Z_{\text{GR}}} \times \frac{1}{1 + \frac{Z_C}{Z_{\text{GR}}}}. \tag{4}$$

In (4), because both $(Z_{\text{outFF}}+Z_{\text{inFF}})$ and Z_C are much larger than Z_{GR}, $A_{\text{VFF}}/(Z_{\text{outFF}} + Z_{\text{injFF}} + Z_C||Z_{\text{GR}})$ is close to but less than one and $1/(1 + Z_C/Z_{\text{GR}})$ is very small. The magnitude of T_{FF} is much smaller than unity and never goes over unity so it is always stable. Based on Fig. 4, the closed-loop transfer function G_{FF} for the FF active filter is derived as

$$G_{\text{FF}}(s) = \frac{I_{\text{RA}}(s)}{I_S(s)} = \frac{G_{\text{OL}}(s)}{1 + G_{\text{OL}}(s) \times \frac{A_{\text{VFF}}(s) + Z_{\text{GR}}}{Z_{\text{outFF}} + Z_{\text{injFF}} - A_{\text{VFF}}(s)}}. \tag{5}$$

The insertion gain is defined as the ratio of the noise current flowing through Z_{GR} with active filters to that without active filters. The lower the insertion gain, the better the active filter performance. The insertion gain for FF configuration is

$$G_{\text{IFF}}(s) = \frac{I_{\text{RA}}(s)}{I_R(s)} = \frac{1}{1 + G_{\text{OL}}(s) \times \frac{A_{\text{VFF}}(s) + Z_{\text{GR}}}{Z_{\text{outFF}} + Z_{\text{injFF}} - A_{\text{VFF}}(s)}}. \tag{6}$$

For the FB active filter in Fig. 2(b), only the reduced signal flow graph is shown in Fig. 5 for brevity. Here, both $Z_{\text{outFB}}+Z_{\text{injFB}}$ and Z_C are much larger than Z_{GR}.

The loop gain for the FB configuration is

$$T_{\text{FB}} = \frac{G_{\text{OL}}}{1 + G_{\text{OL}} \frac{Z_{\text{GR}}}{Z_{\text{outFB}} + Z_{\text{injFB}}}} \times \frac{A_{\text{VFB}}}{Z_{\text{outFB}} + Z_{\text{injFB}}}. \tag{7}$$

The stability of the FB system, based on this loop gain, will be discussed in a later section. Based on Fig. 5, the closed-loop

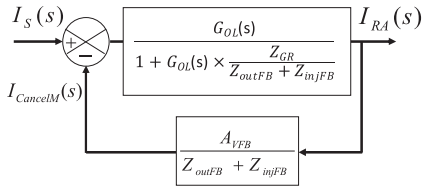

Fig. 5. Reduced signal flow diagram for the FB active filter in Fig. 2(b).

transfer function G_{FB} for the FB active filter is derived as

$$G_{FB}(s) = \frac{I_{RA}(s)}{I_S(s)} = \frac{G_{OL}(s)}{1 + G_{OL}(s) \times \frac{A_{VFB}(s)+Z_{GR}}{Z_{outFB}+Z_{injFB}}}. \quad (8)$$

The insertion gain for the FB configuration is

$$G_{IFB}(s) = \frac{I_{RA}(s)}{I_R(s)} = \frac{1}{1 + G_{OL}(s) \times \frac{A_{VFB}(s)+Z_{GR}}{Z_{outFB}+Z_{injFB}}}. \quad (9)$$

In (9), $(A_{VFB}+Z_{GR})/(Z_{outFB}+Z_{injFB})$ should be as high as possible for the maximum EMI reduction.

III. Investigation of Active Filter Models for FF–FB and FB–FF Configurations

To improve the insertion gain of the single active filters, the FF–FB and FB–FF active filters are investigated in this section. For the FF–FB configuration shown in Fig. 6(a), FF active filter senses the noise current before injection point and FB active filter senses the noise current after the injection point. FF and FB active filters share the same injection point e_{inj1}. For the FB–FF configuration in Fig. 6(b), the two active filters have the same sensed noise current $I_{RB}(s)$ but different injection points. The sensed $I_{RB}(s)$ is amplified and injected at e_{inj1} by the FB active filter and amplified and injected at e_{inj2} by the FF active filter.

A. Closed-Loop Model of FF–FB and FB–FF Configurations

For FF–FB configuration in Fig. 6(a), based on circuit theory, the closed-loop transfer function G_{FF-FB} from current I_S to I_{RA} is (10) shown at the bottom of this page.

Similarly, for the FB–FF configuration in Fig. 6(b), based on circuit theory, the closed-loop transfer function G_{FB-FF} from current I_S to I_{RA} can be derived as (11) shown at the bottom of this page.

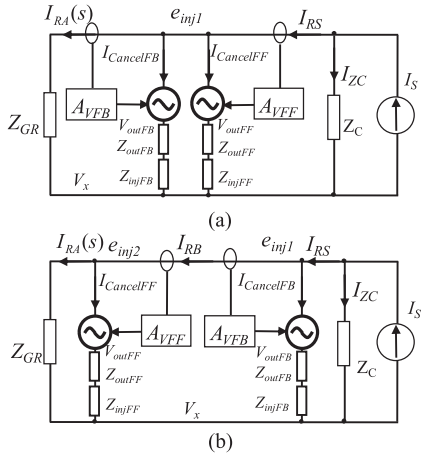

Fig. 6. Active filters in (a) FF–FB and (b) FB–FF configurations along with the Norton equivalent noise model for an ac–dc converter.

The superposition theory is used to derive the loop gains of FF and FB active filters individually. To derive the loop gain $T_{FF/FF-FB}$ of the FF active filter in the FF–FB configuration, based on the superposition theory, let $A_{VFB} = 0$ and $I_S(s) = 0$. The closed-loop output impedance of FB active filter is $Z_{outFB} = Z'_O/(1 + R_G G_{OPC}/(R_G + R_F))$ [3], which is much smaller than Z_{injFB} because of high open-loop gain G_{OPC} of the amplifier and hence is ignored in this derivation. As a result, the load impedance of the FF active filter is $Z_{GR}||Z_{injFB}$ and the source impedance is still Z_C. So, the loop gain is similar to (4) with Z_{GR} replaced by $Z_{GR}||Z_{injFB}$. As discussed before in (4), with this condition, the FF active filter in the FF–FB configuration is always stable.

Next, the loop gain $T_{FB/FF-FB}$ of the FB active filter in the FF–FB configuration and the loop gain $T_{FF/FB-FF}$ of the FF filter and the loop gain $T_{FB/FB-FF}$ of the FB filter in the FB–FF configuration are derived based on the superposition theory. These loop gain equations are listed in Table I. The insertion gain of the whole FF–FB configuration G_{IFF-FB} and the insertion gain of the whole FB–FF configuration G_{IFB-FF} are derived next and listed in Table II .

B. Insertion Gain Improvements

In (9), to minimize the insertion gain, the FB active filter's gain A_{VFB} should be designed large enough so that $A_{VFB} >> Z_{GR}$ and $A_{VFB}/(Z_{outFB}+Z_{injFB}) >> 1$. In (6), for the FF active filter design, to minimize the insertion gain, $A_{VFF}/(Z_{outFF}+Z_{injFF}) \approx 1$. Moreover, with $Z_C \gg Z_{GR}$, $G_{OL}(s) \approx 1$. In the derived insertion

$$G_{FF-FB}(s) = \frac{G_{OL}(s)}{1 + G_{OL}(s) \times \frac{Z_{outFF}+Z_{injFF}}{Z_{outFF}+Z_{injFF}-A_{VFF}} \times \left(\frac{A_{VFB}(s)+Z_r}{Z_{outFB}+Z_{injFB}} + \frac{A_{VFF}(s)+Z_r}{Z_{outFF}+Z_{injFF}}\right)}. \quad (10)$$

$$G_{FB-FF}(s) = \frac{G_{OL}(s)}{1 + G_{OL}(s)\left(\frac{Z_{outFF}+Z_{injFF}+Z_{GR}}{Z_{outFF}+Z_{injFF}-A_{VFF}(s)}\left(\frac{A_{VFF}(s)}{Z_{outFF}+Z_{injFF}} + \frac{A_{VFB}(s)}{Z_{outFB}+Z_{injFB}}\right) + \frac{Z_{GR}}{Z_{outFF}+Z_{injFF}} + \frac{Z_{GR}}{Z_{outFB}+Z_{injFB}}\right)}. \quad (11)$$

TABLE I
LOOP GAIN EXPRESSIONS FOR DIFFERENT CONFIGURATIONS

Loop Gain	Expression
$T_{FB/FF\text{-}FB}$	$\left(\frac{(Z_C \Vert Z_{injFF})/(Z_C \Vert Z_{injFF}+Z_{GR})}{1+(Z_C \Vert Z_{injFF})/(Z_C \Vert Z_{injFF}+Z_{GR})\times Z_{GR}/(Z_{outFB}+Z_{injFB})}\right) \times \left(A_{VFB}/(Z_{outFB}+Z_{injFB})\right)$
$T_{FF/FB\text{-}FF}$	$\frac{-A_{VFF}}{Z_{outFF}+Z_{injFF}+Z_C \Vert Z_{GR} \Vert Z_{injFB}} \times \frac{1}{1+(Z_C \Vert Z_{injFB})/Z_{GR}}$
$T_{FB/FB\text{-}FF}$	$\left(\frac{Z_C/(Z_C+Z_{GR} \Vert Z_{injFF})}{1+Z_C/(Z_C+Z_{GR} \Vert Z_{injFF})\times (Z_{GR} \Vert Z_{injFF})/(Z_{outFB}+Z_{injFB})}\right) \times \left(A_{VFB}/(Z_{outFB}+Z_{injFB})\right)$
$T_{FB1/SFB}$	$\left(\frac{Z_C/(Z_C+Z_{GR} \Vert Z_{inj2})}{1+Z_C/(Z_C+Z_{GR} \Vert Z_{inj2})\times (Z_{GR} \Vert Z_{inj2})/(Z_{out1}+Z_{inj1})}\right) \times \left(A_{VFB1}/(Z_{out1}+Z_{inj1})\right)$
$T_{FB2/SFB}$	$\left(\frac{(Z_C \Vert Z_{inj1})/(Z_C \Vert Z_{inj1}+Z_{GR})}{1+(Z_C \Vert Z_{inj1})/(Z_C \Vert Z_{inj1}+Z_{GR})\times Z_{GR}/(Z_{out2}+Z_{inj2})}\right) \times \left(A_{VFB2}/(Z_{out2}+Z_{inj2})\right)$
$T_{FB1/PFB}$	$\left(\frac{Z_C/(Z_C+Z_{GR} \Vert Z_{inj2})}{1+Z_C/(Z_C+Z_{GR} \Vert Z_{inj2})\times (Z_{GR} \Vert Z_{inj2})/(Z_{out1}+Z_{inj1})}\right) \times \left(A_{VFB1}/(Z_{out1}+Z_{inj1})\right)$
$T_{FB2/PFB}$	$\left(\frac{(Z_C \Vert Z_{inj1})/(Z_C \Vert Z_{inj1}+Z_{GR})}{1+(Z_C \Vert Z_{inj1})/(Z_C \Vert Z_{inj1}+Z_{GR})\times Z_{GR}/(Z_{out2}+Z_{inj2})}\right) \times \left(A_{VFB2}/(Z_{out2}+Z_{inj2})\right)$

TABLE II
INSERTION GAIN EXPRESSIONS FOR DIFFERENT CONFIGURATIONS

Insertion Gain	Expression
$G_{IFF\text{-}FB}$	$\frac{1}{1+\frac{G_{OL}\times(Z_{outFF}+Z_{injFF})}{(Z_{outFF}+Z_{injFF}-A_{VFF})}\left(\frac{A_{VFB}+Z_{GR}}{Z_{outFB}+Z_{injFB}}+\frac{A_{VFF}+Z_{GR}}{Z_{outFF}+Z_{injFF}}\right)}$
$G_{IFB\text{-}FF}$	$1/\left(1+G_{OL}\times\left(\frac{(Z_{outFF}+Z_{injFF}+Z_{GR})}{(Z_{outFF}+Z_{injFF}-A_{VFF})}\left(\frac{A_{VFF}}{Z_{outFF}+Z_{injFF}}+\frac{A_{VFB}}{Z_{outFB}+Z_{injFB}}\right)+\frac{Z_{GR}}{Z_{outFF}+Z_{injFF}}+\frac{Z_{GR}}{Z_{outFB}+Z_{injFB}}\right)\right)$
G_{ISFB}	$\frac{1}{1+G_{OL}\times\left(\frac{A_{VFB1}+Z_{GR}}{Z_{out1}+Z_{inj1}}+\frac{A_{VFB2}+Z_{GR}}{Z_{out2}+Z_{inj2}}+\left(\frac{A_{VFB1}}{Z_{out1}+Z_{inj1}}\times\frac{A_{VFB2}+Z_{GR}}{Z_{out2}+Z_{inj2}}\right)\right)}$
G_{IPFB}	$\frac{1}{1+G_{OL}\times\left(\frac{A_{VFB1}+Z_{GR}}{Z_{out1}+Z_{inj1}}+\frac{A_{VFB2}+Z_{GR}}{Z_{out2}+Z_{inj2}}\right)}$

gains G_{IFF-FB} and G_{IFB-FF} in Table II, when $Z_{outFF}+Z_{injFF}$-A_{VFF} ≈ 0, the insertion gain is the minimum.

Because $A_{VFB}(s)/(Z_{outFB}+Z_{injFB})>>A_{VFF}(s)/(Z_{outFF}+Z_{injFF})$ and $A_{VFB}>>Z_{GR}$, the insertion gains G_{IFF-FB} and G_{IFB-FF} in Table II are almost the same and the improvement over single FB filter in (9) mostly depends on the multiplication term $1/(Z_{outFF}+Z_{injFF}$-$A_{VFF})$, which comes from the FF active filter. Hence, the insertion gain improvement of FF–FB and FB–FF configurations mostly depends on the FF active filter but due to the tolerance of the component values, significant improvement in performance is difficult. Because with the FB configuration the performance does not depend on the accuracy of component values, multiple FB configurations will be investigated in the next section.

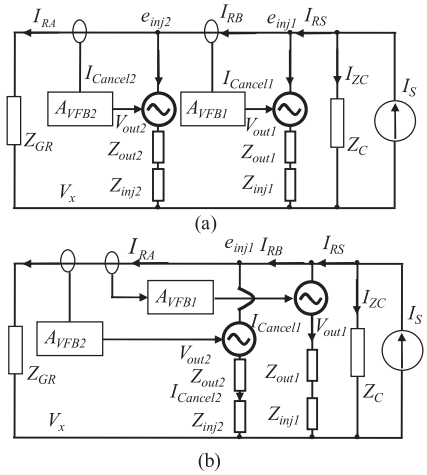

Fig. 7. Active filters in multiple FB configurations. (a) SFB and (b) PFB.

IV. INVESTIGATION OF MULTIPLE FB CONFIGURATIONS: SFB AND PFB

SFB and PFB configurations will be investigated here to improve the FB active filter's performance.

A. Closed-Loop Models of SFB and PFB Configurations

SFB and PFB configurations are shown in Fig. 7(a) and (b), respectively. A_{VFB1}, $I_{Cancel1}$, V_{out1}, Z_{out1}, and Z_{inj1} are the parameters of the first FB active filter FB1 and A_{VFB2}, $I_{Cancel2}$, V_{out2}, Z_{out2}, and Z_{inj2} are the parameters of the second FB active filter FB2. For the SFB configuration in Fig. 7(a), the two active filters have different injection points: e_{inj1} for FB1 and e_{inj2} for FB2. The noise currents sensed by the FB1 and FB2 are $I_{RB}(s)$ and $I_{RA}(s)$, respectively. For PFB, FB1 and FB2 active filters share the same injection point e_{inj1}, as shown in Fig. 7(b), and both filters sense the same noise current $I_{RA}(s)$. Based on Fig. 7(a), the closed-loop transfer function for the SFB configuration can be derived as (12) shown at the bottom of this page.

Similarly, based on Fig. 7(b), the closed-loop transfer function for PFB configuration can be derived as

$$G_{PFB}(s)=\frac{G_{OL}(s)}{1+G_{OL}(s)\left(\frac{A_{VFB1}(s)+Z_{GR}}{Z_{out1}+Z_{inj1}}+\frac{A_{VFB2}(s)+Z_{GR}}{Z_{out2}+Z_{inj2}}\right)}. \quad (13)$$

Next, the loop gain $T_{FB1/SFB}$ of FB1 in SFB configuration, the loop gain $T_{FB2/SFB}$ of FB2 in SFB configuration, the loop gain $T_{FB1/PFB}$ of FB1 in PFB configuration, and the loop gain $T_{FB2/PFB}$ of FB2 in PFB configuration are derived based on the superposition theory similarly to the method used in the

$$G_{SFB}(s)=\frac{G_{OL}(s)}{1+G_{OL}(s)\left(\frac{A_{VFB1}(s)+Z_{GR}}{Z_{out1}+Z_{inj1}}+\frac{A_{VFB2}(s)+Z_{GR}}{Z_{out2}+Z_{inj2}}+\left(\frac{A_{VFB1}(s)}{Z_{out1}+Z_{inj1}}\times\frac{A_{VFB2}(s)+Z_{GR}}{Z_{out2}+Z_{inj2}}\right)\right)}. \quad (12)$$

previous section. These loop gain equations are listed in Table I. The insertion gains of the SFB and PFB configurations, G_{ISFB} and G_{IPFB}, respectively, are also derived and listed in Table II.

B. Insertion Gain Improvements

Comparing the insertion gains G_{ISFB} and G_{IPFB} in Table II, it is found that in the denominator of G_{ISFB} there is a multiplication term, $(\frac{A_{\mathrm{VFB1}}(s)}{Z_{\mathrm{out1}}+Z_{\mathrm{inj1}}} \times \frac{A_{\mathrm{VFB2}}(s)+Z_{\mathrm{GR}}}{Z_{\mathrm{out2}}+Z_{\mathrm{inj2}}})$, which is not present in G_{IPFB}. For the SFB active filter, because the insertion gain G_{ISFB} is mainly determined by the product of A_{VFB1} and A_{VFB2} in the denominator, G_{ISFB} is much smaller than G_{IFB}. In the denominator of G_{IPFB}, the gains of the two active filters are only added; hence, even though G_{IPFB} is lower than G_{IFB}, G_{ISFB} gives much better attenuation than G_{IPFB}, as it best utilizes the gains of both the active filters through multiplication.

V. Comparison of Insertion Gains and Loop Gains of the Configurations and Stability Analysis

The loop gains and stability of the active filter configurations derived in previous sections will be explored and compared in this section.

The parameters of the used passive filter and boost converter component are: Z_{LDM} is $L_{\mathrm{DM}} = 71\ \mu$H, with $R_{\mathrm{LDM}} = 5.42\ \mathrm{k}\Omega$ and $C_{\mathrm{LDM}} = 6.1$ pF in parallel. The DM impedance Z_{LDMCM} of the CM inductor is $L_{\mathrm{DMCM}} = 23.6\ \mu$H with $R_{\mathrm{LDMCM}} = 3\ \mathrm{k}\Omega$ and $C_{\mathrm{LDMCM}} = 0.28$ nF in parallel. The impedance of the boost inductor Z_B is $L_B = 327\ \mu$H, with $R_{\mathrm{LB}} = 2.97\ \mathrm{k}\Omega$ and $C_{\mathrm{LB}} = 9.44$ nF in parallel. The two passive capacitors are $C_{\mathrm{DM}} = 0.47\ \mu$F and $C_R = 0.47\ \mu$F. Damping resistors $R_{\mathrm{CDM}} = 5\ \Omega$ and $R_{\mathrm{CR}} = 1\ \Omega$ are used in series with C_{DM} and C_R, respectively, to eliminate the low frequency resonance caused by DM capacitors and inductors.

For both the FF and FB active filter circuits, the OPAM used is AD829, a conventional voltage FB amplifier, which has a wide unity gain bandwidth of 120 MHz and high rail to rail voltage (±15 V), which is good for high output voltage swing. The two transistors T_1 and T_2 in the class AB amplifier in Fig. 3 are a matched n-p-n–p-n-p complementary transistor pair ZDT6753. For the CT design, the magnetic core used is ZJ42106TC from Magnetics company. The key circuit parameters for FF and FB active filters in Fig. 3 are given as follows.

FF Active Filter:

CT: $n = 10$, $L_{\mathrm{CT}} = 2$ mH, $R_{\mathrm{CT}} = 10\ \Omega$, $C_{\mathrm{HP}} = 10\ \mu$F

OPAM: $R_{\mathrm{G}} = 100\ \Omega$, $R_F = 820\ \Omega$, $C_{\mathrm{inj}} = 0.47\ \mu$F, $R_{\mathrm{inj}} = 20\ \Omega$, $R_o = 20\ \Omega$, $G_o = 7000$, $\omega_{\mathrm{OP1}} = 2\pi \times 104$r/s, $\omega_{\mathrm{OP2}} = 2\pi \times 30 \times 106$ rad/s

Class AB: $\beta_0 = 150$, $C_{\mathrm{BE}} = 300$ pF, $C_{\mathrm{BC}} = 30$ pF, $r_{\mathrm{BE}} = 543\ \Omega$, $R_{E1} = R_{E2} = 5\ \Omega$, $R_{B1} = R_{B2} = 4.7\ \mathrm{k}\Omega$

FB Active Filter:

CT: $n = 10$, $L_{\mathrm{CT}} = 2$ mH, $R_{\mathrm{CT}} = 30\ \Omega$, $C_{\mathrm{HP}} = 10\ \mu$F

OPAM: $R_G = 100\ \Omega$, $R_F = 985\ \Omega$, $C_{\mathrm{inj}} = 0.47\ \mu$F, $R_{\mathrm{inj}} = 5\ \Omega$, $R_o = 20\ \Omega$, $G_o = 7000$, $\omega_{\mathrm{OP1}} = 2\pi \times 104$ r/s, $\omega_{\mathrm{OP2}} = 2\pi \times 30 \times 106$ rad/s

Class AB: Same as FF

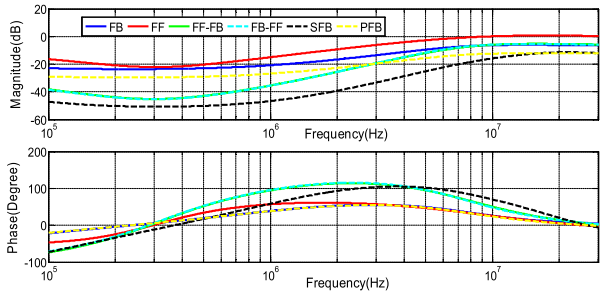

Fig. 8. Comparison of insertion gains for FF, FB, FF–FB, FB–FF, SFB, and PFB configurations.

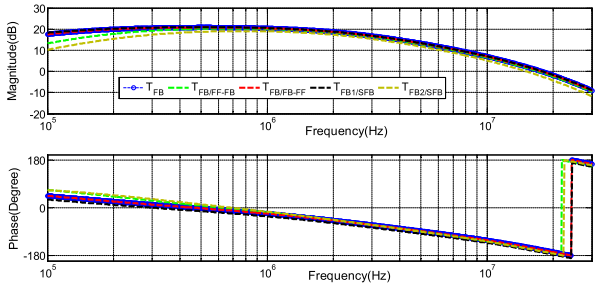

Fig. 9. Loop gain comparison: T_{FB}, $T_{\mathrm{FB/FF-FB}}$, $T_{\mathrm{FB/FB-FF}}$, $T_{\mathrm{FB1/SFB}}$, and $T_{\mathrm{FB2/SFB}}$.

For the FB active filter, R_G and R_F are designed to have 20-dB gain for the OPAM. Based on (2) and (9), R_{CT} and R_{inj} can be designed so that the insertion gain from the FB active filter is close to –20 dB in pass band from 150 kHz. Similarly, for the FF active filter, based on (2) and (6), R_G, R_F, R_{CT}, and R_{inj} are designed so that the insertion gain from the FF active filter is close to –20 dB. Other parameters of FF and FB active filter are the same. The details of how to design the parameters of CT, OPAM, and class AB amplifier for a single FB active filter are described in [33]. Based on these parameters, the calculated insertion gains are shown in Fig. 8. It is shown that the SFB configuration gives the lowest insertion gain as expected. Both the FF–FB and FB–FF configurations give the same insertion gain as explained before.

The calculated loop gains for all FB active filters are shown in Fig. 9. PFB loop gains $T_{\mathrm{FB1/PFB}}$ and $T_{\mathrm{FB2/PFB}}$ are not shown as they are exactly same as $T_{\mathrm{FB1/SFB}}$ and $T_{\mathrm{FB2/SFB}}$. The loop gains for FF active filters are not shown here too as they are much lower than 0 dB and always stable. The FB loop gains T_{FB}, $T_{\mathrm{FB/FF-FB}}$, $T_{\mathrm{FB/FB-FF}}$, $T_{\mathrm{FB1/SFB}}$, and $T_{\mathrm{FB2/SFB}}$ have very small phase margins at crossover between 10 and 20 MHz due to the OPAM's HF poles. Based on (2) and (7), A_{VFB} is a factor of T_{FB} and $V_{\mathrm{out}}/V_{\mathrm{in}}$ is a factor of A_{VFB}. At HF, $V_{\mathrm{out}}/V_{\mathrm{in}}$ can be expressed as follows:

$$\frac{V_{\mathrm{out}}}{V_{\mathrm{in}}} \approx \frac{A_{\mathrm{NI}}}{1 + \frac{s}{Q\omega_{\mathrm{UC}}} + \left(\frac{s}{\omega_{\mathrm{UC}}}\right)^2} \tag{14}$$

where $\omega_{\mathrm{UC}} = \sqrt{\frac{G_o\omega_{\mathrm{OP1}}\omega_{\mathrm{OP2}}}{A_{\mathrm{NI}}}}$, $Q\omega_{\mathrm{UC}} = \frac{G_o\omega_{\mathrm{OP1}}}{A_{\mathrm{NI}}}$, and the noninverting amplifier gain $A_{\mathrm{NI}} = 1 + R_F/R_G$. The double pole ω_{UC} introduces an abrupt –180° change. Because there are

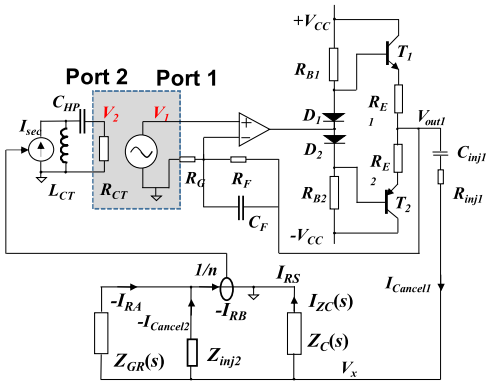

Fig. 10. Loop gain measurement for one active filter in an SFB by breaking one of the FB loops.

parasitic poles that are not included in (7) above 30 MHz from the amplifier, the phase margin of the loop gain is very small at the crossover frequency in Fig. 9. If this double pole is split to two faraway separated single poles, the phase will change slowly across several decades, and enough phase margin could be achieved. By paralleling a small capacitor C_F with the FB resistor R_F, as shown in Fig. 10, the double pole can be split to two separate single poles. $V_{\text{out}}/V_{\text{in}}$ can now be approximately represented as

$$\frac{V_{\text{out}}}{V_{\text{in}}} \approx \frac{A_{\text{NI}}\left(1+\frac{s}{\omega_{\text{CZ}}}\right)}{\left(1+\frac{s}{\omega_{\text{CP1}}}\right)\left(1+\frac{s}{\omega_{\text{CP2}}}\right)\left(1+\frac{s}{\omega_{\text{CP3}}}\right)} \tag{15}$$

where $\omega_{\text{CZ}} = \omega_{\text{PF}} A_{\text{NI}}$, $\omega_{\text{PF}} = 1/(R_F C_F)$, $\omega_{\text{CP1}} = 1/(A_{\text{NI}}/(G_o\omega_{\text{OP1}}) + (1/\omega_{\text{PF}}))$, $\omega_{\text{CP2}} = \omega_{\text{OP2}}(1 + (G_o\omega_{\text{OP1}})/(A_{\text{NI}}\omega_{\text{PF}}))$. The value of the capacitor C_F is designed to make ω_{CP3} very close to ω_{CZ} so they cancel each other. In the next section, only SFB active filters will be discussed in detail for brevity.

VI. Experimental Results

A. Loop Gain Measurement and Stability Analysis

Two separate FB active filter prototypes with the same specifications in Section V were developed following the circuit of Fig. 3. These two units were used in an SFB or PFB configuration with a boost PFC ac–dc converter. The boost PFC converter is UCC28180EVM-573 from Texas Instruments with ac input range 85–265 V_{AC}. Its maximum output power is 360 W, and rated output voltage is 390 V. It has fixed 120 kHz switching frequency. The FB loop was broken between the HPF and OPAM of active filter FB1 [3], [23] in the SFB configuration of Fig. 7(a). The S-parameters were measured between ports 1 and 2, as shown in Fig. 10. The loop gain was derived from the measured S-parameters [30] based on source impedance ($\approx R_{\text{CT}}$) and load impedance ($\approx R_G$) at breaking point. The similar setup can be applied to FB2 and the PFB configuration in Fig. 7(b). The S-parameters were measured using a network analyzer Copper Mountain Planar 808/1.

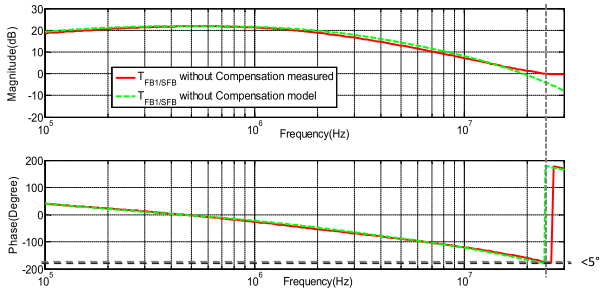

Fig. 11. Loop gain comparison $T_{\text{FB1/SFB}}$ (uncompensated).

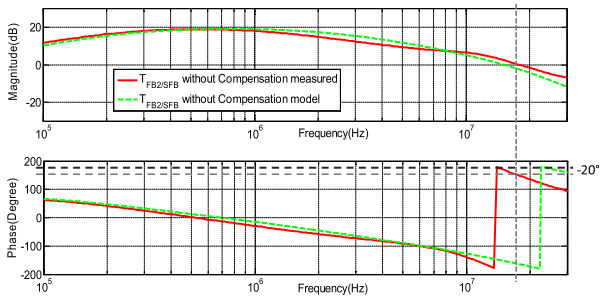

Fig. 12. Loop gain comparison $T_{\text{FB2/SFB}}$ (uncompensated).

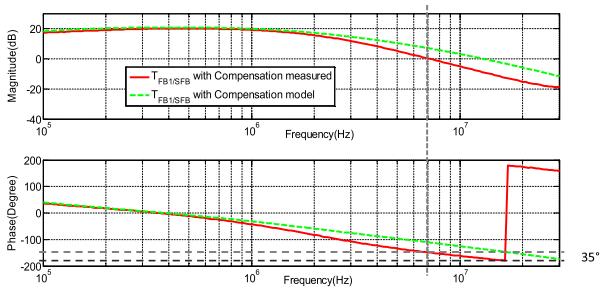

Fig. 13. Loop gain comparison $T_{\text{FB1/SFB}}$ (compensated).

The measured and modeled $T_{\text{FB1/SFB}}$ and $T_{\text{FB2/SFB}}$ are compared in Figs. 11 and 12, respectively. It is shown that $T_{\text{FB1/SFB}}$ has less than +5° phase margin around 23 MHz and $T_{\text{FB2/SFB}}$ has –20° phase margin around 17 MHz.

To increase the phase margin in $T_{\text{FB1/SFB}}$, based on the technique described in (15), a small capacitor $C_F = 33$ pF is paralleled with the FB resistor R_F of FB1 circuit. Similarly, a capacitor $C_F = 100$ pF is paralleled with the FB resistor R_F of FB2 circuit in $T_{\text{FB2/SFB}}$. After the compensation, the measured and modeled loop gains for $T_{\text{FB1/SFB}}$ and $T_{\text{FB2/SFB}}$ are shown in Figs. 13 and 14, respectively. In Fig. 13, $T_{\text{FB1/SFB}}$ has a phase margin of around 35° and in Fig. 14, $T_{\text{FB2/SFB}}$ has a phase margin of around 40°.

B. Insertion Gain Measurement and Comparison

The insertion gain was also derived from the measured S-parameters [3], [28], [30] in another measurement setup. Different from Fig. 10, the FB loop was not broken but Z_{GR} and Z_C are replaced with the two ports of the network analyzer. The

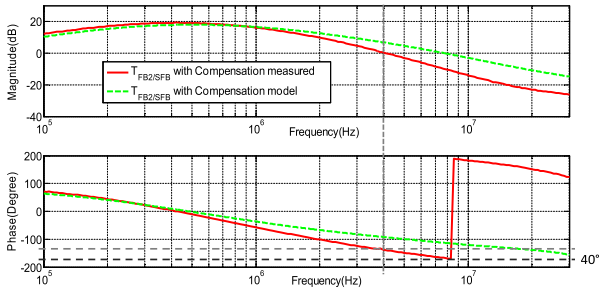

Fig. 14. Loop gain comparison $T_{\mathrm{FB2/SFB}}$ (compensated).

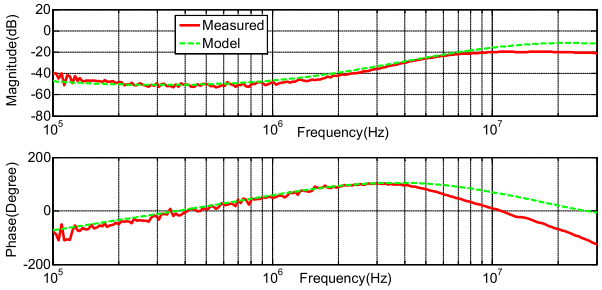

Fig. 15. Comparison of the modeled and measured SFB insertion gains.

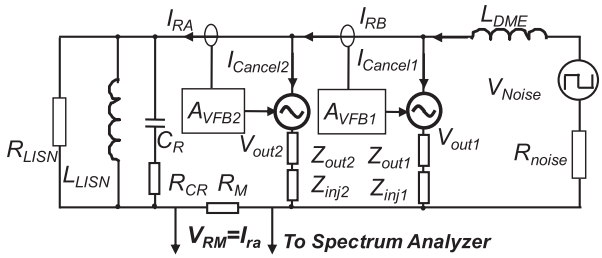

Fig. 16. Measurement setup with a square wave voltage source from an RF amplifier as the noise source.

measured and modeled insertion gains are compared in Fig. 15 for SFB active filter and they match well.

C. Spectrum Measurements

In the first experiment, the noise is a square wave voltage source in series with a 50 Ω impedance from an RF amplifier. The measurement setup for the SFB configuration with a spectrum analyzer is shown in Fig. 16. In Fig. 16, a DM inductor $L_{\mathrm{DME}} = 200\ \mu$H, whose impedance is much higher than 50 Ω in the concerned frequency range, is used to emulate the noise source impedance Z_C in Fig. 1(b). A passive filter capacitor C_R of 0.47 μF in series with a damping resistance $R_{\mathrm{CR}} = 1\ \Omega$ is in parallel with the LISNs to meet the impedance mismatch requirement [1]. The spectrum analyzer measures the noise current I_{RA} by measuring the voltage across a small resistance $R_M = 1\ \Omega$. R_{LISN} and L_{LISN} are the simplified model of LISNs.

The noise current spectra without active filter, with single FB active filter and with SFB active filter, are compared in Fig. 17. The fundamental frequency of the square wave was 100 kHz.

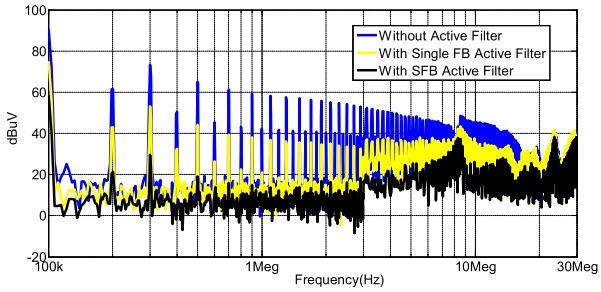

Fig. 17. Comparison of the measured DM noise: without active filters, with single FB active filter, and with the SFB active filter.

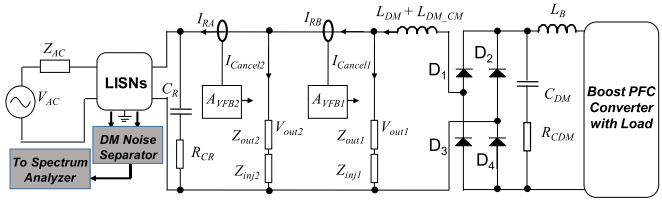

Fig. 18. Experimental setup with a boost PFC ac–dc converter.

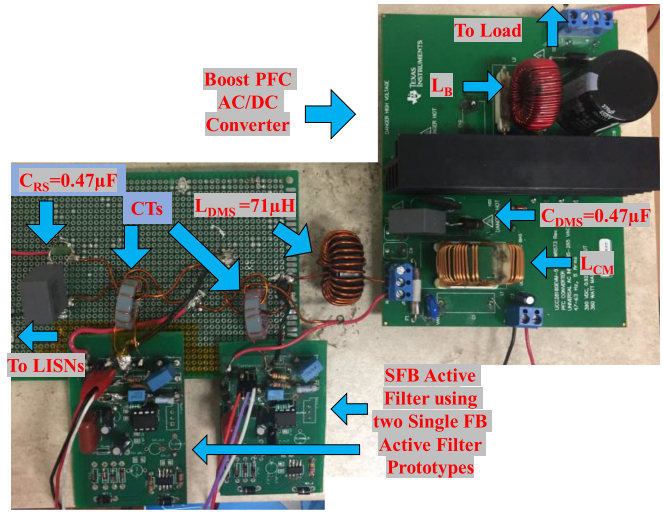

Fig. 19. Photograph of the experimental setup with the boost PFC ac–dc converter and the SFB active filter.

It is shown that, compared with the passive filter without the active filter, the single FB active filter with the passive filter can reduce EMI by up to 20 dB, and the SFB active filter with the passive filter achieved up to more than 40-dB attenuation with stable operation from 100 kHz to beyond 20 MHz.

In the second experiment, the SFB active filter was tested with a commercial boost PFC ac–dc converter. The experimental setup is shown in Fig. 18. The photograph of the experimental setup with SFB active EMI filter along with the boost PFC converter is shown in Fig. 19. The converter has a switching frequency of 120 kHz with 170 W output power. DM spectrum measurement results without and with the SFB active filter are shown in Fig. 20. The SFB active filter achieved around 45-dB attenuation at low frequencies with stable operation.

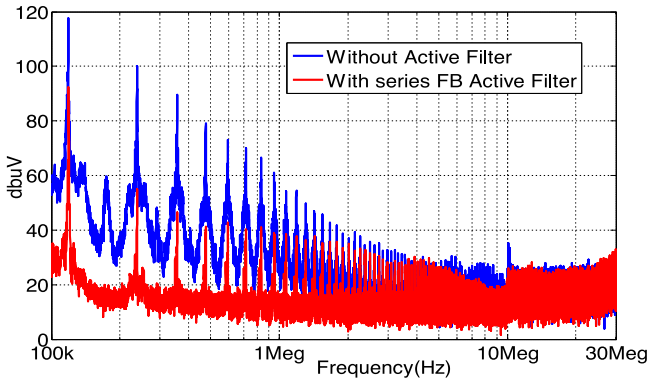

Fig. 20. Comparison of the measured DM noise: without active filters and with the SFB active filter.

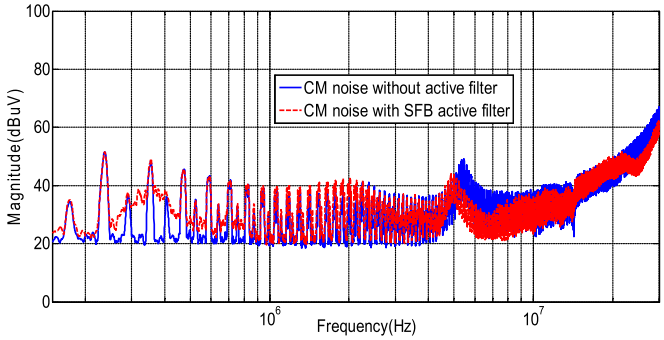

Fig. 21. Comparison of the measured CM noise: without any active filters and with the SFB active filter.

The DM active filter does not change the CM noise current in the system. The CM noise current is the displacement current flowing through the parasitic capacitance between the high *dv/dt* nodes in the converter and the ground due to high *dv/dt*. The DM active filter injects cancelation current between two power lines. It does not inject any current to the ground and it does not change *dv/dt* of the converter, so the active filter does not change the CM noise. In a similar experimental setup to that in Fig. 18 with a CM noise separator [31], measured CM noise without and with the active filter is shown in Fig. 21, which also proves the analysis.

As discussed previously, the active filter can reduce the EMI in low frequency range and a small passive filter can achieve the remaining attenuation requirement in HF range, so the passive filter size could be reduced. The modeling techniques, control strategies, and theoretical analysis developed in this paper are very useful in practical active DM EMI filter design for ac–dc or dc/ac converters. An active filter can be designed following the guideline below. At first, the bare DM EMI noise spectrum is measured without any EMI filters. Second, the attenuation requirement for the EMI filter is determined based on the measured bare noise and EMI standards. Third, the attenuation requirement is divided upon the active filter and the small passive filter based on desired attenuation profile. Both the passive filter and the active filter will be designed based on the attenuation requirements. The filter model including the passive filter, active filter, and ac–dc power converter will be developed. Based on the developed model, the FB loop of the active filter will be designed to have the desired attenuation and stability. Finally, a prototype will be built, and EMI measurement will be conducted to validate the design. A practically designed DM active EMI filter can greatly reduce the size of the passive filter [33] and hence the developed SFB active filter topology, with its much higher attenuation compared to the single FB active filter, should be able to further reduce the overall size of the EMI filter.

VII. Conclusion

The DM EMI active filter design for ac–dc converters was a challenging task due to the presence of line frequency voltage or current components in the sensed noise, which needs to be rejected from the injected current/voltage. Due to the requirement of low gain at line frequency and high gain at EMI frequencies and associated stability constraints, the performance of the single active filters as found in the available literature was not good. In this paper, for DM EMI noise of an ac–dc converter, single FB and single FF active filter models, which included a noise source, a passive filter, and a load, were first developed. Second, to improve the performance of the single active filters, the models, insertion gain, and loop gain equations of FF–FB, FB–FF, PFB, and SFB active filters were developed, analyzed, and compared for the first time in the available literature. Compensation techniques were developed to ensure stability. Based on the analysis and comparison of the models of these active filter configurations, this paper developed a solution to overcome the low insertion gain issue of single FB active DM EMI filter based on the developed SFB active filter model. The models developed in this paper were validated through experiments and it is shown that they can correctly predict active filter's performance and stability. The performance improvement of the developed SFB configuration was verified in EMI measurement, which shows that an SFB active filter has significantly better performance than a single FB active filter.

References

[1] S. Wang, Y. Y. Maillet, F. Wang, D. Boroyevich, and R. Burgos, "Investigation of hybrid EMI filters for common-mode EMI suppression in a motor drive system," *IEEE Trans. Power Electron.*, vol. 25, no. 4, pp. 1034–1045, Apr. 2010.

[2] J. Biela, A. Wirthmueller, R. Waespe, M. L. Heldwein, K. Raggl, and J. W. Kolar, "Passive and active hybrid integrated EMI filters," *IEEE Trans. Power Electron.*, vol. 24, no. 5, pp. 1340–1349, May 2009.

[3] Y. Chu, S. Wang, and Q. Wang, "Modeling and stability analysis of active/hybrid common-mode EMI filters for dc–dc power converters," *IEEE Trans. Power Electron.*, vol. 31, no. 9, pp. 6254–6263, Sep. 2016.

[4] D. Hamza, M. Sawan, and P. K. Jain, "Suppression of common-mode input electromagnetic interference noise in DC-DC converters using the active filtering method," *IET Trans. Power Electron.*, vol. 4, no. 7, pp. 776–784, Aug. 2011.

[5] M. C. Di Piazza, A. Ragusa, and G. Vitale, "An optimized feedback common mode active filter for vehicular induction motor drives," *IEEE Trans. Power Electron.*, vol. 26, no. 11, pp. 3153–3162, Nov. 2011.

[6] W. Chen, X. Yang, J. Xue, and F. Wang, "A novel filter topology with active motor CM impedance regulator in PWM ASD system," *IEEE Trans. Ind. Electron.*, vol. 61, no. 12, pp. 6938–6946, Dec. 2014.

[7] P. Pairodamonchai, S. Suwankawin, and S. Sangwongwanich, "Design and implementation of a hybrid output EMI filter for high-frequency common-mode voltage compensation in PWM inverters," *IEEE Trans. Ind. Appl.*, vol. 45, no. 5, pp. 1647–1659, Sep./Oct. 2009.

[8] M. Hartmann, H. Ertl, and J. W. Kolar, "EMI filter design for a 1 MHz, 10 kW three-phase/level PWM rectifier," *IEEE Trans. Power Electron.*, vol. 26, no. 4, pp. 1192–1204, Apr. 2011.
[9] W. Chen, X. Yang, and Z. Wang, "Systematic evaluation of hybrid active EMI filter based on equivalent circuit model," in *Proc. 37th IEEE Power Electron. Spec. Conf.*, Jeju, South Korea, 2006, pp. 1–7.
[10] M. C. Di Piazza, G. Tine, and G. Vitale, "An improved active common-mode voltage compensation device for induction motor drives," *IEEE Trans. Ind. Electron.*, vol. 55, no. 4, pp. 1823–1834, Apr. 2008.
[11] M. C. Di Piazza, A. Ragusa, and G. Vitale, "Effects of common-mode active filtering in induction motor drives for electric vehicles," *IEEE Trans. Veh. Technol.*, vol. 59, no. 6, pp. 2664–2673, Jul. 2010.
[12] D. Shin *et al.*, "Analysis and design guide of active EMI filter in a compact package for reduction of common-mode conducted emissions," *IEEE Trans. Electromagn. Compat.*, vol. 57, no. 4, pp. 660–671, Aug. 2015.
[13] W. Chen, X. Yang, and Z. Wang, "Analysis of insertion loss and impedance compatibility of hybrid EMI filter based on equivalent circuit model," *IEEE Trans. Ind. Electron.*, vol. 54, no. 4, pp. 2057–2064, Aug. 2007.
[14] D. Hamza, M. Qiu, and P. K. Jain, "Application and stability analysis of a novel digital active EMI filter used in a grid-tied PV microinverter module," *IEEE Trans. Power Electron.*, vol. 28, no. 6, pp. 2867–2874, Jun. 2013.
[15] W. Chen, X. Yang, and Z. Wang, "An active EMI filtering technique for improving passive filter low-frequency performance," *IEEE Trans. Electromagn. Compat.*, vol. 48, no. 1, pp. 172–177, Feb. 2006.
[16] M. C. Di Piazza, M. Luna, A. Ragusa, and G. Vitale, "An improved common mode active filter for EMI reduction in vehicular motor drives," in *Proc. IEEE Veh. Power Propulsion Conf.*, Chicago, IL, USA, 2011, pp. 1–8.
[17] W. Chen, W. Zhang, X. Yang, Z. Sheng, and Z. Wang, "An experimental study of common- and differential-mode active EMI filter compensation characteristics," *IEEE Trans. Electromagn. Compat.*, vol. 51, no. 3, pp. 683–691, Aug. 2009.
[18] M. Ali, E. Laboure, and F. Costa, "Integrated active filter for differential-mode noise suppression," *IEEE Trans. Power Electron.*, vol. 29, no. 3, pp. 1053–1057, Mar. 2014.
[19] N. K. Poon, J. C. P. Liu, C. K. Tse, and M. H. Pong, "Techniques for input ripple current cancellation: Classification and implementation [in SMPS]," *IEEE Trans. Power Electron.*, vol. 15, no. 6, pp. 1144–1152, Nov. 2000.
[20] D. C. Hamill, "An efficient active ripple filter for use in DC-DC conversion," *IEEE Trans. Aerosp. Electron. Syst.*, vol. 32, no. 3, pp. 1077–1084, Jul. 1996.
[21] T. Farkas and M. F. Schlecht, "Viability of active EMI filters for utility applications," *IEEE Trans. Power Electron.*, vol. 9, no. 3, pp. 328–337, May 1994.
[22] R. Goswami, S. Wang, and Y. Chu, "Modeling and analysis of hybrid differential mode filters for ac–dc converters to suppress current ripples and EMI," in *Proc. IEEE Energy Convers. Congr. Expo.*, Montreal, QC, Canada, 2015, pp. 2429–2436.
[23] R. Goswami, S. Wang, and Y. Chu, "Design of an active differential mode current filter for a boost power factor correction AC-DC converter," in *Proc. IEEE Energy Convers. Congr. Expo.*, Montreal, QC, Canada, 2015, pp. 4375–4382.
[24] R. Goswami, S. Wang, and Y. Zhang, "Modeling, analysis and design of differential mode active EMI filters with feedforward and feedback configurations for AC-DC converters," in *Proc. IEEE Energy Convers. Congr. Expo.*, Milwaukee, WI, USA, 2016, pp. 1–8.
[25] M. Zhu, D. J. Perreault, V. Caliskan, T. C. Neugebauer, S. Guttowski, and J. G. Kassakian, "Design and evaluation of feedforward active ripple filters," *IEEE Trans. Power Electron.*, vol. 20, no. 2, pp. 276–285, Mar. 2005.
[26] K. Raggl, T. Nussbaumer, and J. W. Kolar, "Guideline for a simplified differential-mode EMI filter design," *IEEE Trans. Ind. Electron.*, vol. 57, no. 3, pp. 1031–1040, Mar. 2010.
[27] S. Wang, F. C. Lee, and W. G. Odendaal, "Improving the performance of boost PFC EMI filters," in *Proc. 18th Annu. IEEE Appl. Power Electron. Conf. Expo.*, Miami Beach, FL, USA, 2003, vol. 1, pp. 368–374.
[28] S. Wang, F. C. Lee, and W. G. Odendaal, "Characterization and parasitic extraction of EMI filters using scattering parameters," *IEEE Trans. Power Electron.*, vol. 20, no. 2, pp. 502–510, Mar. 2005.
[29] S. Wang, P. Kong, and F. C. Lee, "Common mode noise reduction for boost converters using general balance technique," *IEEE Trans. Power Electron.*, vol. 22, no. 4, pp. 1410–1416, Jul. 2007.
[30] S. Wang, F. C. Lee, and W. G. Odendaal, "Using scattering parameters to characterize EMI filters," in *Proc. IEEE 35th Annu. Power Electron. Spec. Conf.*, 2004, vol. 1, pp. 297–303.
[31] S. Wang, F. C. Lee, and W. G. Odendaal, "Characterization, evaluation, and design of noise separator for conducted EMI noise diagnosis," *IEEE Trans. Power Electron.*, vol. 20, no. 4, pp. 974–982, Jul. 2005.
[32] R. Goswami and S. Wang, "Modeling and stability analysis of active differential-mode EMI filters for ac–dc power converters," *IEEE Trans. Power Electron.*, vol. 33, no. 12, pp. 10277–10291, Dec. 2018.
[33] R. Goswami, S. Wang, E. Solodovnik, and K. Karimi, "Differential mode active EMI filter design for a boost power factor correction (PFC) ac–dc converter," *IEEE J. Emerg. Sel. Topics Power Electron.*, to be published, doi: 10.1109/JESTPE.2018.2839734.

Rajib Goswami (S'11) received the B.Sc. Engineering and M.Sc. Engineering degrees in electrical and electronic engineering from the Bangladesh University of Engineering and Technology, Dhaka, Bangladesh, in 2009 and 2012, respectively, and the Ph.D. degree in electrical engineering from the University of Texas at San Antonio, San Antonio, TX, USA, in 2017.

He is currently a Senior Engineer with the Bangladesh Atomic Energy Commission, Dhaka, Bangladesh. He was with the power electronics and electrical power research laboratory (PEEPRL) of the University of Florida as a Research Intern. His research interests include hybrid(active/passive) EMI filter design for DM/CM noise of power converters, EMI noise analysis and filter design for three-phase converters, power conversion from wind turbine generators (maximum power tracking), etc.

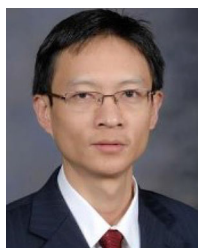

Shuo Wang (S'03–M'06–SM'07–F'19) received the Ph.D. degree in electrical engineering from Virginia Tech, Blacksburg, VA, USA, in 2005.

Since 2015, he has been an Associate Professor with the Department of Electrical and Computer Engineering, University of Florida, Gainesville, FL, USA. From 2010 to 2014, he was with the University of Texas at San Antonio, San Antonio, TX, USA, first as an Assistant Professor and later as an Associate Professor. From 2009 to 2010, he was a Senior Design Engineer with the GE Aviation Systems, Vandalia, OH, USA. From 2005 to 2009, he was a Research Assistant Professor with Virginia Tech. He has authored or coauthored more than 160 IEEE journal and conference papers and holds eight U.S. patents.

Dr. Wang was the recipient of the Best Transaction Paper Award from the IEEE Power Electronics Society in 2006, two William M. Portnoy Awards for the papers published in the IEEE Industry Applications Society in 2004 and 2012, and the prestigious National Science Foundation CAREER Award in 2012. He is an Associate Editor for the IEEE TRANSACTIONS ON INDUSTRY APPLICATIONS and a Technical Program Co-Chair for the IEEE 2014 International Electric Vehicle Conference.